Advances in Nano Research, *Vol. 19, No. 4 (2025) 335-346*
https://doi.org/10.12989/anr.2025.19.4.335

Stability analysis and optimization management of nanocomposites-reinforced panels using a thickness-dependent shear deformation theory and HDQM

Suleiman Ibrahim Mohammad*[1,2], Sultan Alaswad Alenazi[3], Hanan Jadallah[1], Badrea Al Oraini[4],
Asokan Vasudevan[5,6], Khaled Mohamed Elhadi[7,8] and Murat Yaylacı[9,10]

[1]*Electronic Marketing and Social Media, Economic and Administrative Sciences Zarqa University, Jordan*
[2]*Research follower, INTI International University, 71800 Negeri Sembilan, Malaysia*
[3]*Marketing Department, College of Business, King Saud University, Riyadh 11362, Saudi Arabia*
[4]*Department of Business Administration, Collage of Business and Economics, Qassim University, Qassim, Saudi Arabia*
[5]*Faculty of Business and Communications, INTI International University, 71800 Negeri Sembilan, Malaysia*
[6]*Shinawatra University, 99 Moo 10, Bangtoey, Samkhok, Pathum Thani 12160 Thailand*
[7]*Civil Engineering Department, College of Engineering, King Khalid University, Saudi Arabia*
[8]*Center for Engineering and Technology Innovations, King Khalid University, Abha 61421, Saudi Arabia*
[9]*Department of Civil Engineering, Recep Tayyip Erdogan University, 53100, Rize, Turkey*
[10]*Turgut Kıran Maritime Faculty, Recep Tayyip Erdogan University, 53900, Rize, Turkey*

(*Received February 28, 2022, Revised August 18, 2025, Accepted September 12, 2025*)

Abstract. Using the modified couple stress theory, this study investigates the nonlinear vibrations of a sandwich microshell composed of a functionally graded graphene platelets (FG-GPL)-reinforced core and two uniform outer skins, all simply supported. The analysis employs the first-order shear deformation shell theory alongside a nonlinear strain framework. The mechanical properties of the GPL-reinforced core are assumed to vary with thickness, utilizing the Halpin-Tsai model. Three distinct distribution patterns of GPLs throughout the thickness are examined. The microshell is subjected to thermal loading, facilitating the calculation of its temperature field across the thickness by applying the one-dimensional Fourier heat conduction equation, which accounts for thermal boundary conditions at both the inner and outer surfaces of the shell. The shell models incorporate shear deformation and rotary inertia, while geometric nonlinearity is addressed using the von Karman approach. The fundamental partial differential equations (PDEs) governing the system are derived using Hamilton's principle. These coupled PDEs are then transformed into a set of ordinary differential equations (ODEs) via the Galerkin method and solved using the multiple timescale method to obtain results. The findings are validated against existing literature, demonstrating a robust level of agreement. This study thoroughly examines the effects of various factors, including GPL weight fraction, thickness distribution patterns, material length scale parameters, core length, radius, and individual layer thickness on nonlinear frequency ratios, fundamental linear frequencies, and nonlinear frequencies.

Keywords: functionally graded graphene platelets; nonlinear vibration; sandwich shells; size dependent; thermal influence

1. Introduction

Nanocomposites have emerged in recent years as a new and exciting class of materials in modern engineering design that offers significant improvements to mechanical, thermal, and electrical properties relative to traditional composites (Rashvand *et al.* 2022, Forooghi *et al.* 2023, Safaei *et al.* 2023). The addition of nanoparticles (CNTs, graphene, nanoclay) into the matrix material enhances the overall performance of the composite material and makes it perfect for challenging engineering applications (Lu *et al.* 2025). These materials typically have better strength-to-density ratios, higher stiffness, better thermal conductivity, and better corrosion and wear resistance than traditional composites (Li and Liu 2025). Nanocomposites are now indispensable in tough engineering environments such as aerospace, automotive, and civil engineering, where material performance is paramount (Hoang and Thanh 2024). The improved mechanical properties of nanocomposites allow companies to design lighter and ultimately more efficient structures in order to maximize fuel efficiency and reduce operating costs in the aerospace and automotive industries (Babaei *et al.* 2024). The improved thermal properties make them ideal candidates for use in areas where temperatures fluctuate and heat must be dissipated, such as in electronic devices and high-performance coatings (Mahinzare *et al.* 2024). The electrical conductivity of certain nanocomposites could also lead to the development of sensors, batteries, and conductive films, aiding in the development of electronics and energy storage technology (Avcar *et al.* 2023). In addition, the multifunctionality of nanocomposites allows them to meet the sustained and durable requirements of engineering design (Ebrahimi and Salari 2018). Generally, nanocomposites have better resistance to environmental degradation, which may elongate the necessity for maintenance and replacement of engineered systems (Jayakumari *et al.* 2024). It is worth considering the

---

*Corresponding author, Ph.D.,
E-mail: dr.sliman@yahoo.com

http://www.techno-press.org/?journal=journal=anr&subpage=5 ISSN: 2287-237X (Print), 2287-2388 (Online)

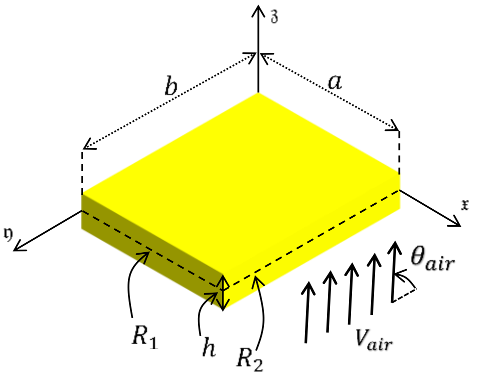

Fig. 1 A schematic view of the doubly curved panel in terms of airflow loading

possibility of ‘smart’ materials that possess self-healing, sensing, or adaptable systems made possible through the introduction of nanocomposites, leading to potentially adaptive structures used in critical infrastructure (Shen *et al.* 2024). While attractive alternatives for engineering design, the use of nanocomposites presents challenges related to cost, processing techniques, and scale (Xia *et al.* 2023). However, with continued research in nanotechnology and advancements in manufacturing, these challenges are being confronted (Arshid *et al.* 2023). With time, mature development of nanocomposites will lead to their increased development in advanced engineering design displacing traditional materials with a performance, durability, and efficiency that could cultivate new concepts across multiple diverse applications (Arshid *et al.* 2023). To prepare for the future needs of humanity, study and future applications of nanotechnologies and nanocomposites in engineering design must be pursued (Davoise *et al.* 2023).

Stability analysis is one of the most critical parts of engineering design, and provides a major contribution to ensuring the safety, reliability, and performance of structures and systems subjected to various loading conditions (Boutaleb *et al.* 2024, Bousmaha *et al.* 2025). The design of a well-functioning, robust, and efficient system depends heavily on the ability to predict how materials and structures will behave under different stresses, such as axial loads, bending, torsion, and shear (Gawah *et al.* 2025). Stability analysis helps to identify critical points of failure, which can occur with thin-walled structures (sudden buckling) or dynamic systems that experience vibrations or vibrational instabilities (Youzera *et al.* 2025a). By evaluating failure modes, engineers can leverage the designs to mitigate catastrophic breakdowns and improve the useful life of structures (Youzera *et al.* 2025b). In civil and mechanical engineering, stability analysis is critical for safely designing buildings, bridges, and other structures that are subjected to dynamic forces, such as wind load, earthquake load, or traffic load (Al-Houri *et al.* 2024). In applying stability principles, the designer can, with confidence, determine that structures will not experience excessive deformations due to extreme external forces that would restrict or prevent safe operations (Tounsi *et al.* 2024). In aerospace engineering, stability analysis becomes even more important because of the extreme degradation of stability experienced by even minor deviations from stable behavior produced by aircraft and spacecraft (Zerrouki *et al.* 2024). Stability analysis is not limited to traditional engineering disciplines, it is also important for automotive and marine systems, where vibration, shock loading, and aerodynamic forces can compromise structural integrity (Alsubaie *et al.* 2024). The analysis of thermal stability is equally important for many high-performance systems where overheating can lead to failure, such as engines or electronic devices. Furthermore, stability analysis gives engineers the ability to predict the behavior of composite materials that are becoming increasingly applied in modern engineering by virtue of their increased strength-to-weight ratio and customizability (Viola *et al.* 2013).

For the first time, this paper provides an extensive study of the stability and optimization management of nanocomposite-reinforced doubly curved panels under varying airflow speed and airflow angle. In modeling the panels, the objects are modeled as two-dimensional membrane structures, however, their complex deformation behavior is represented using the thickness-dependent shear deformation theory. The panels are subjected to aerodynamic loading, and the HDQM is utilized as a numerical tool to solve the governing equations with high accuracy, allowing for reliable predictions of the panel’s dynamic stability. The nanocomposite material used CNT reinforcement, which was modeled using the rule of mixtures to obtain the effective properties of the nanocomposite. The elastic behavior was modeled utilizing Hooke’s law, and the governing equations of motion were obtained through Hamilton’s principle. The study assessed the structural stability of the panels under airflow characteristics, including airflow speed and angle. The change in airflow conditions demonstrates the effect of the dynamics of aerodynamic loading in relation to buckling and vibration behavior of nanocomposite-reinforced doubly curved panels. The paper also presents an optimization framework that minimizes the instability of the structure and maximizes performance if the geometry and material contents of the panels are varied according to structural demands. The findings of the study indicate that the presence of CNTs improves the structural integrity and stability of doubly curved panels, suggesting that optimal performance can be achieved in positively affecting the dynamic stability of curved panels with varying stiffness properties.

2. Effective material properties of CNTRCs

Fig. 1 presents a schematic view of the doubly curved panel in terms of airflow loading. The curvature of the panel is defined by two principal radii, R_1, R_2, that typify the complex geometry of the shell. An airstream with a velocity being the vector V_{air} is flowing over the surface of the panel. This airstream induces a distributed pressure load over the surface of the panel. When a panel is subjected to an airstream, it induces structural deformation and vibrations. In this example, the coordinate ‘$\mathfrak{x}$’ provides a spatial axis for which the panel’s responses can be modeled. It is important to note that this figure presents a coupled fluid-structure interaction problem, which is relevant for aviation and mechanical engineering considerations regarding the aeroelastic stability and dynamics of curved panels.

Three different methods are suggested to replicate the distribution of single-walled carbon nanotubes (SWCNTs) across the structure's thickness in the model that is being shown. Formulations based on the well-known rule of mixtures (ROM) are used to calculate the effective thermomechanical characteristics for the FG-SWCNT reinforced nanocomposite material, taking into account the efficiency factor related to SWCNTs (Safarpour and Alibeigloo 2021).

$$E_{11}=\eta_1 \mathrm{v}_{\mathrm{CNT}} E_{11}^{\mathrm{CNT}}+\mathrm{v}_{\mathrm{m}} E^{\mathrm{m}}, \tag{1a}$$

$$\frac{\eta_2}{E_{22}}=\frac{\mathrm{v}_{\mathrm{CNT}}}{E_{22}^{\mathrm{CNT}}}+\frac{\mathrm{v}_{\mathrm{m}}}{E^{m}}, \tag{1b}$$

$$\frac{\eta_3}{G_{12}}=\frac{\mathrm{v}_{\mathrm{CNT}}}{G_{12}^{\mathrm{CNT}}}+\frac{\mathrm{v}_{\mathrm{m}}}{G^{\mathrm{m}}}, \tag{1c}$$

$$\nu_{12}=\mathrm{v}_{\mathrm{CNT}}^{*} \nu_{12}^{\mathrm{CNT}}+\mathrm{v}_{\mathrm{m}} \nu^{\mathrm{m}}, \tag{1d}$$

$$\rho=\mathrm{v}_{\mathrm{CNT}} \rho^{\mathrm{CNT}}+\mathrm{v}_{\mathrm{m}} \rho^{\mathrm{m}}, \tag{1e}$$

As stated in Ref. (Liu *et al*. 2021), the following formula will be developed to relate v_{m} and v_{CNT}.

$$\mathrm{v}_{\mathrm{CNT}}+\mathrm{v}_{\mathrm{m}}=1 \tag{2}$$

The following formulas are given as (Safarpour and Alibeigloo 2021) in order to mathematically depict the volume fraction of each SWCNT dispersion paradigm across the structure's thickness.

$$\begin{gathered}\text{FG-X: } \mathrm{v}_{\mathrm{CNT}}=4\mathrm{v}_{\mathrm{CNT}}^{*}\left|\frac{\mathfrak{z}}{h}\right|, \\ \text{FG-O: } \mathrm{v}_{\mathrm{CNT}}=2\mathrm{v}_{\mathrm{CNT}}^{*}\left(1-2\left|\frac{\mathfrak{z}}{h}\right|\right), \\ \text{FG-UD: } \mathrm{v}_{\mathrm{CNT}}=\mathrm{v}_{\mathrm{CNT}}^{*}, \\ \text{FG-V: } \mathrm{v}_{\mathrm{CNT}}=\mathrm{v}_{\mathrm{CNT}}^{*}\left(1+2\frac{\mathfrak{z}}{h}\right),\end{gathered} \tag{3}$$

v_{CNT}^{*} can be presented by the following formulation:

$$\mathrm{v}_{\mathrm{CNT}}^{*}=\frac{W_{\mathrm{CNT}}}{W_{\mathrm{CNT}}+(\frac{\rho^{\mathrm{CNT}}}{\rho^{\mathrm{M}}})(1\text{-}\mathrm{W}_{\mathrm{CNT}})} \tag{4}$$

The weight content of SWCNT is shown here by W_{CNT}. The relationship between the nanocomposite structure's other thermomechanical characteristics is expressed as follows.

$$\mathrm{v}_{21}=\frac{E_{22}}{E_{11}}\mathrm{v}_{12}, \ \mathrm{G}_{12}=\mathrm{G}_{13}=\mathrm{G}_{23}. \tag{5}$$

The shells employed here have material properties derived from (Safarpour and Alibeigloo 2021).

3. Vibration theoretical model

The current study analyzes the vibration behavior of the CNTRC doubly curved panel under airflow pressure by first deriving the governing equations using the FSDT. The shell structures' displacement field is displayed as follows (Reddy 2003):

$$\mathfrak{U}(\mathfrak{x},\mathfrak{y},\mathfrak{z},\mathrm{t})=\mathbb{u}(\mathfrak{x},\mathfrak{y},\mathrm{t})+\mathfrak{z}\not{f}_{\mathfrak{x}}(\mathfrak{x},\mathfrak{y},\mathrm{t}), \tag{6a}$$

$$\mathfrak{V}(\mathfrak{x},\mathfrak{y},\mathfrak{z},\mathrm{t})=\mathbb{v}(\mathfrak{x},\mathfrak{y},\mathrm{t})+\mathfrak{z}\not{f}_{\mathfrak{y}}(\mathfrak{x},\mathfrak{y},\mathrm{t}), \tag{6b}$$

$$\mathfrak{W}(\mathfrak{x},\mathfrak{y},\mathfrak{z},\mathrm{t})=\mathbb{w}(\mathfrak{x},\mathfrak{y},\mathrm{t}). \tag{6c}$$

The variable $\mathbb{u}$ represents the center surface displacement along the $\mathfrak{x}$-axis inside the plane, and the variables $\mathbb{v}$ and $\mathbb{w}$ represent the displacements along the $\mathfrak{y}$- and $\mathfrak{z}$-axes, respectively. Furthermore, the variables $\not{f}_{\mathfrak{x}}$ and $\not{f}_{\mathfrak{y}}$, respectively, show the rotational displacement components around the $\mathfrak{y}$-axis and $\mathfrak{x}$-axis. Any position displacement field can be modeled using shear and transverse strain-displacement interactions:

$$\begin{gathered}\begin{Bmatrix}\varepsilon_{\mathfrak{x}}\\ \varepsilon_{\mathfrak{y}}\\ \gamma_{\mathfrak{x}\mathfrak{y}}\end{Bmatrix}=\begin{Bmatrix}\frac{\partial\mathbb{u}}{\partial\mathfrak{x}}+\frac{\mathbb{w}}{R_1}+\mathfrak{z}\frac{\partial\not{f}_{\mathfrak{x}}}{\partial\mathfrak{x}}\\ \frac{\partial\mathbb{v}}{\partial\mathfrak{y}}+\frac{\mathbb{w}}{R_2}+\mathfrak{z}\frac{\partial\not{f}_{\mathfrak{y}}}{\partial\mathfrak{y}}\\ \frac{\partial\mathbb{u}}{\partial\mathfrak{y}}+\frac{\partial\mathbb{v}}{\partial\mathfrak{x}}+\mathfrak{z}\frac{\partial\not{f}_{\mathfrak{x}}}{\partial\mathfrak{y}}+\mathfrak{z}\frac{\partial\not{f}_{\mathfrak{y}}}{\partial\mathfrak{x}}\end{Bmatrix}\\ \begin{Bmatrix}\gamma_{\mathfrak{x}\mathfrak{z}}\\ \gamma_{\mathfrak{y}\mathfrak{z}}\end{Bmatrix}=\begin{Bmatrix}\not{f}_{\mathfrak{x}}+\frac{\partial\mathbb{w}}{\partial\mathfrak{x}}-\frac{\mathbb{u}}{R_1}\\ \not{f}_{\mathfrak{y}}+\frac{\partial\mathbb{w}}{\partial\mathfrak{y}}-\frac{\mathbb{v}}{R_2}\end{Bmatrix}\end{gathered} \tag{7}$$

where $\gamma_{\mathfrak{x}\mathfrak{y}}$, $\gamma_{\mathfrak{x}\mathfrak{z}}$ and $\gamma_{\mathfrak{y}\mathfrak{z}}$ represent the shear components of strain, while $\varepsilon_{\mathfrak{x}}$ and $\varepsilon_{\mathfrak{y}}$ represent the normal components of strain. Furthermore, Hooke's law explains the connection between stress and strain in the CNTRC doubly curved panel:

$$\begin{gathered}\begin{Bmatrix}\sigma_{\mathfrak{x}}\\ \sigma_{\mathfrak{y}}\\ \tau_{\mathfrak{x}\mathfrak{y}}\end{Bmatrix}=\begin{bmatrix}\mathbb{Q}_{11} & \mathbb{Q}_{12} & 0\\ \mathbb{Q}_{12} & \mathbb{Q}_{22} & 0\\ 0 & 0 & \mathbb{Q}_{66}\end{bmatrix}\begin{Bmatrix}\varepsilon_{\mathfrak{x}}\\ \varepsilon_{\mathfrak{y}}\\ \gamma_{\mathfrak{x}\mathfrak{y}}\end{Bmatrix},\\ \begin{Bmatrix}\tau_{\mathfrak{y}\mathfrak{z}}\\ \tau_{\mathfrak{x}\mathfrak{z}}\end{Bmatrix}=\begin{bmatrix}\mathbb{Q}_{44} & 0\\ 0 & \mathbb{Q}_{55}\end{bmatrix}\begin{Bmatrix}\gamma_{\mathfrak{y}\mathfrak{z}}\\ \gamma_{\mathfrak{x}\mathfrak{z}}\end{Bmatrix}\end{gathered} \tag{8}$$

Moreover, the following is an expression for the stiffness coefficient utilized in Eq. (8):

$$\begin{gathered}\mathbb{Q}_{11}=\frac{E_{11}}{1-\nu_{12}\nu_{21}},\ \mathbb{Q}_{22}=\frac{E_{22}}{1-\nu_{12}\nu_{21}},\ \mathbb{Q}_{12}=\frac{E_{11}\nu_{21}}{1-\nu_{12}\nu_{21}},\\ \mathbb{Q}_{44}=G_{23},\ \mathbb{Q}_{55}=G_{13},\ \mathbb{Q}_{66}=G_{12}.\end{gathered} \tag{9}$$

The following is what the Hamilton principle (Reddy, 2003) states:

$$\int_0^{\mathrm{t}}\delta(U+V-K)d\mathrm{t}=0 \tag{10}$$

where the variational operator is denoted by δ. The change in strain energy, δU, of the CNTRC doubly curved panel can be described as follows:

$$\begin{aligned}\delta U&=\int_{\mathbb{V}}\left(\sigma_{\mathfrak{x}}\delta\varepsilon_{\mathfrak{x}}+\sigma_{\mathfrak{y}}\delta\varepsilon_{\mathfrak{y}}+\tau_{\mathfrak{x}\mathfrak{y}}\delta\gamma_{\mathfrak{x}\mathfrak{y}}+\tau_{\mathfrak{y}\mathfrak{z}}\delta\gamma_{\mathfrak{y}\mathfrak{z}}+\tau_{\mathfrak{x}\mathfrak{z}}\delta\gamma_{\mathfrak{x}\mathfrak{z}}\right)d\mathbb{V}\\ &=\int_A\quad(\mathfrak{N}_{\mathfrak{x}}(\frac{\partial\delta\mathbb{u}}{\partial\mathfrak{x}}+\frac{\delta\mathbb{w}}{R_1})+\mathfrak{N}_{\mathfrak{y}}(\frac{\partial\delta\mathbb{v}}{\partial\mathfrak{y}}+\frac{\delta\mathbb{w}}{R_2})\end{aligned} \tag{11}$$

$$+\mathfrak{N}_{\mathfrak{x}\mathfrak{y}}\left(\frac{\partial\delta\mathbb{u}}{\partial\mathfrak{x}}+\frac{\partial\delta\mathbb{v}}{\partial\mathfrak{y}}\right)+\mathfrak{M}_{\mathfrak{x}}\frac{\partial\delta\phi_{\mathfrak{x}}}{\partial\mathfrak{x}}+\mathfrak{M}_{\mathfrak{y}}\frac{\partial\delta\phi_{\mathfrak{y}}}{\partial\mathfrak{y}}$$
$$+\mathfrak{M}_{\mathfrak{x}\mathfrak{y}}\left(\frac{\partial\delta\phi_{\mathfrak{x}}}{\partial\mathfrak{x}}+\frac{\partial\delta\phi_{\mathfrak{y}}}{\partial\mathfrak{y}}\right)+\mathbb{Q}_{\mathfrak{x}\mathfrak{z}}\left(\delta\phi_{\mathfrak{x}}+\frac{\partial\delta\mathbb{w}}{\partial\mathfrak{x}}-\frac{\delta\mathbb{u}}{R_1}\right)$$
$$+\mathbb{Q}_{\mathfrak{y}\mathfrak{z}}(\delta\phi_{\mathfrak{y}}+\frac{\partial\delta\mathbb{w}}{\partial\mathfrak{y}}-\frac{\delta\mathbb{v}}{R_2}))dA$$

The constants $\mathfrak{N}_{\mathfrak{x}}, \mathfrak{N}_{\mathfrak{y}}$, and $\mathfrak{N}_{\mathfrak{x}\mathfrak{y}}$ stand for the membrane forces, $\mathfrak{M}_{\mathfrak{x}}, \mathfrak{M}_{\mathfrak{y}}$, and $\mathfrak{M}_{\mathfrak{x}\mathfrak{y}}$ for the bending moments, and $\mathbb{Q}_{\mathfrak{x}\mathfrak{z}}, \mathbb{Q}_{\mathfrak{y}\mathfrak{z}}$ for the shear forces in the doubly curved panel. The following formulas can be used to represent these variables:

$$\begin{Bmatrix}\mathfrak{N}_{\mathfrak{x}}\\ \mathfrak{N}_{\mathfrak{y}}\\ \mathfrak{N}_{\mathfrak{x}\mathfrak{y}}\end{Bmatrix}=\int_{-\frac{h}{2}}^{h/2}\begin{Bmatrix}\sigma_{\mathfrak{x}}\\ \sigma_{\mathfrak{y}}\\ \tau_{\mathfrak{x}\mathfrak{y}}\end{Bmatrix}d\mathfrak{z},$$
$$\begin{Bmatrix}\mathfrak{M}_{\mathfrak{x}}\\ \mathfrak{M}_{\mathfrak{y}}\\ \mathfrak{M}_{\mathfrak{x}\mathfrak{y}}\end{Bmatrix}=\int_{-\frac{h}{2}}^{h/2}\mathfrak{z}\begin{Bmatrix}\sigma_{\mathfrak{x}}\\ \sigma_{\mathfrak{y}}\\ \tau_{\mathfrak{x}\mathfrak{y}}\end{Bmatrix}d\mathfrak{z}, \tag{12}$$
$$\begin{Bmatrix}\mathbb{Q}_{\mathfrak{x}\mathfrak{z}}\\ \mathbb{Q}_{\mathfrak{y}\mathfrak{z}}\end{Bmatrix}=\int_{-h/2}^{h/2}\begin{Bmatrix}\tau_{\mathfrak{x}\mathfrak{z}}\\ \tau_{\mathfrak{y}\mathfrak{z}}\end{Bmatrix}d\mathfrak{z}$$

When airflow pressure loading causes a change in work, δV can be written as follows:

$$\delta V=-\int_A \mathscr{q}_{\mathfrak{z}}\frac{\partial^2\mathbb{w}}{\partial\mathfrak{x}^2}\delta\mathbb{w}dA \tag{13}$$

where:

$$\mathscr{q}_{\mathfrak{z}}=\tfrac{1}{2}\rho_{air}V_{air}^2 sin(\theta_{air}). \tag{14}$$

θ_{air} and V_{air} stand for the wind attack angle and average wind speed, respectively, the air density, represented by ρ_{air}, is taken to be $\rho_{air}=1.235$ [kg/m^3] (Nguyen *et al*. 2024). The component of δK can be identified using the following:

$$\delta K=\int_v(\dot{\mathfrak{U}}\delta\dot{\mathfrak{U}}+\dot{\mathfrak{V}}\delta\dot{\mathfrak{V}}+\dot{\mathfrak{W}}\delta\dot{\mathfrak{W}})\,\rho d\mathbb{V} \tag{15}$$

The following information is provided by the variables $(\mathcal{J}_1,\mathcal{J}_2,\mathcal{J}_3)$, which represent the inertial mass components inside the doubly curved panel:

$$(\mathcal{J}_1,\mathcal{J}_2,\mathcal{J}_3)=\int_{-h/2}^{h/2}\rho\,(1,\mathfrak{z},\mathfrak{z}^2)d\mathfrak{z}. \tag{16}$$

Eqs. (11), (13), and (15) can be substituted into Eq. (10), which may yield the governing equation of motion:

$$\delta\mathbb{u}:\ \frac{\partial\mathfrak{N}_{\mathfrak{x}}}{\partial\mathfrak{x}}+\frac{\partial\mathfrak{N}_{\mathfrak{x}\mathfrak{y}}}{\partial\mathfrak{y}}+\frac{\mathbb{Q}_{\mathfrak{x}\mathfrak{z}}}{R_1}=\mathcal{J}_1\frac{\partial^2\mathbb{u}}{\partial\mathfrak{t}^2}+\mathcal{J}_2\frac{\partial^2\phi_{\mathfrak{x}}}{\partial\mathfrak{t}^2}, \tag{17a}$$

$$\delta\mathbb{v}:\ \frac{\partial\mathfrak{N}_{\mathfrak{y}}}{\partial\mathfrak{y}}+\frac{\partial\mathfrak{N}_{\mathfrak{x}\mathfrak{y}}}{\partial\mathfrak{x}}+\frac{\mathbb{Q}_{\mathfrak{y}\mathfrak{z}}}{R_2}=\mathcal{J}_1\frac{\partial^2\mathbb{v}}{\partial\mathfrak{t}^2}+\mathcal{J}_2\frac{\partial^2\phi_{\mathfrak{y}}}{\partial\mathfrak{t}^2}, \tag{17b}$$

$$\delta\mathbb{w}:\ \frac{\partial\mathbb{Q}_{\mathfrak{x}\mathfrak{z}}}{\partial\mathfrak{x}}+\frac{\partial\mathbb{Q}_{\mathfrak{y}\mathfrak{z}}}{\partial\mathfrak{y}}-\frac{\mathfrak{N}_{\mathfrak{x}}}{R_1}-\frac{\mathfrak{N}_{\mathfrak{y}}}{R_2}-\mathscr{q}_{\mathfrak{z}}=\mathcal{J}_1\frac{\partial^2\mathbb{w}}{\partial\mathfrak{t}^2}, \tag{17c}$$

$$\delta\phi_{\mathfrak{x}}:\ \frac{\partial\mathfrak{M}_{\mathfrak{x}}}{\partial\mathfrak{x}}+\frac{\partial\mathfrak{M}_{\mathfrak{x}\mathfrak{y}}}{\partial\mathfrak{y}}-\mathbb{Q}_{\mathfrak{x}\mathfrak{z}}=\mathcal{J}_2\frac{\partial^2\mathbb{u}}{\partial\mathfrak{t}^2}+\mathcal{J}_3\frac{\partial^2\phi_{\mathfrak{x}}}{\partial\mathfrak{t}^2}, \tag{17d}$$

$$\delta\phi_{\mathfrak{y}}:\ \frac{\partial\mathfrak{M}_{\mathfrak{y}}}{\partial\mathfrak{y}}+\frac{\partial\mathfrak{M}_{\mathfrak{x}\mathfrak{y}}}{\partial\mathfrak{x}}-\mathbb{Q}_{\mathfrak{y}\mathfrak{z}}=\mathcal{J}_2\frac{\partial^2\mathbb{v}}{\partial\mathfrak{t}^2}+\mathcal{J}_3\frac{\partial^2\phi_{\mathfrak{y}}}{\partial\mathfrak{t}^2}. \tag{17e}$$

Furthermore, Eqs. (17a), (17b), (17c), (17d), and (17e) can be further reformulated as follows using Eqs. (12), (16).

$$\begin{gathered}\delta\mathbb{u}:\ \mathcal{A}_{11}\frac{\partial^2\mathbb{u}}{\partial\mathfrak{x}^2}+\mathcal{A}_{66}\frac{\partial^2\mathbb{u}}{\partial\mathfrak{y}^2}-\frac{\mathcal{A}_{55}\mathbb{u}}{R_1^2}+\mathcal{A}_{12}\frac{\partial^2\mathbb{v}}{\partial\mathfrak{x}\partial\mathfrak{y}}+\\ \mathcal{A}_{66}\frac{\partial^2\mathbb{v}}{\partial\mathfrak{x}\partial\mathfrak{y}}+\frac{\mathcal{A}_{11}}{R_1}\frac{\partial\mathbb{w}}{\partial\mathfrak{x}}+\mathcal{A}_{12}\frac{\partial\mathbb{w}}{R_2\partial\mathfrak{x}}+\frac{\mathcal{A}_{55}}{R_1}\frac{\partial\mathbb{w}}{\partial\mathfrak{x}}+\mathbb{B}_{11}\frac{\partial^2\phi_{\mathfrak{x}}}{\partial\mathfrak{x}^2}+\\ \mathbb{B}_{66}\frac{\partial^2\phi_{\mathfrak{x}}}{\partial\mathfrak{y}^2}+\frac{\mathcal{A}_{55}\phi_{\mathfrak{x}}}{R_1}+\mathbb{B}_{12}\frac{\partial^2\phi_{\mathfrak{y}}}{\partial\mathfrak{x}\partial\mathfrak{y}}+\mathbb{B}_{66}\frac{\partial^2\phi_{\mathfrak{y}}}{\partial\mathfrak{x}\partial\mathfrak{y}}=\mathcal{J}_1\frac{\partial^2\mathbb{u}}{\partial\mathfrak{t}^2}+\\ \mathcal{J}_2\frac{\partial^2\phi_{\mathfrak{x}}}{\partial\mathfrak{t}^2},\end{gathered} \tag{18a}$$

$$\begin{gathered}\delta\mathbb{v}:\ \mathcal{A}_{12}\frac{\partial^2\mathbb{u}}{\partial\mathfrak{x}\partial\mathfrak{y}}+\mathcal{A}_{66}\frac{\partial^2\mathbb{u}}{\partial\mathfrak{x}\partial\mathfrak{y}}+\mathcal{A}_{22}\frac{\partial^2\mathbb{v}}{\partial\mathfrak{y}^2}+\mathcal{A}_{66}\frac{\partial^2\mathbb{v}}{\partial\mathfrak{x}^2}-\\ \frac{\mathcal{A}_{44}\mathbb{v}}{R_2^2}+\frac{\mathcal{A}_{12}\partial\mathbb{w}}{R_1\partial\mathfrak{y}}+\frac{\mathcal{A}_{22}}{R_2}\frac{\partial\mathbb{w}}{\partial\mathfrak{y}}+\frac{\mathcal{A}_{44}}{R_2}\frac{\partial\mathbb{w}}{\partial\mathfrak{y}}+\mathbb{B}_{12}\frac{\partial^2\phi_{\mathfrak{x}}}{\partial\mathfrak{x}\partial\mathfrak{y}}+\\ \mathbb{B}_{66}\frac{\partial^2\phi_{\mathfrak{x}}}{\partial\mathfrak{x}\partial\mathfrak{y}}+\mathbb{B}_{22}\frac{\partial^2\phi_{\mathfrak{y}}}{\partial\mathfrak{y}^2}+\mathbb{B}_{66}\frac{\partial^2\phi_{\mathfrak{y}}}{\partial\mathfrak{x}^2}+\frac{\mathcal{A}_{44}\phi_{\mathfrak{y}}}{R_2}=\mathcal{J}_1\frac{\partial^2\mathbb{v}}{\partial\mathfrak{t}^2}+\\ \mathcal{J}_2\frac{\partial^2\phi_{\mathfrak{y}}}{\partial\mathfrak{t}^2},\end{gathered} \tag{18b}$$

$$\begin{gathered}\delta\mathbb{w}:\ -\left(\frac{(\mathcal{A}_{11}+\mathcal{A}_{55})}{R_1}+\frac{\mathcal{A}_{12}}{R_2}\right)\frac{\partial\mathbb{u}}{\partial\mathfrak{x}}-\left(\frac{(\mathcal{A}_{22}+\mathcal{A}_{44})}{R_2}+\right.\\ \left.\frac{\mathcal{A}_{12}}{R_1}\right)\frac{\partial\mathbb{v}}{\partial\mathfrak{y}}+(\frac{\mathcal{A}_{11}}{R_1^2}+\frac{\mathcal{A}_{22}}{R_2^2}+\frac{2\mathcal{A}_{12}}{R_1R_2})\mathbb{w}+\mathcal{A}_{55}\frac{\partial^2\mathbb{w}}{\partial\mathfrak{x}^2}+\\ \mathcal{A}_{44}\frac{\partial^2\mathbb{w}}{\partial\mathfrak{y}^2}-\mathscr{q}_{\mathfrak{z}}\frac{\partial^2\mathbb{w}}{\partial\mathfrak{x}^2}+\mathcal{A}_{55}\frac{\partial\phi_{\mathfrak{x}}}{\partial\mathfrak{x}}-(\frac{\mathbb{B}_{11}}{R_1}+\frac{\mathbb{B}_{12}}{R_2})\frac{\partial\phi_{\mathfrak{x}}}{\partial\mathfrak{x}}+\\ \mathcal{A}_{44}\frac{\partial\phi_{\mathfrak{y}}}{\partial\mathfrak{y}}-(\frac{\mathbb{B}_{12}}{R_1}+\frac{\mathbb{B}_{22}}{R_2})\frac{\partial\phi_{\mathfrak{y}}}{\partial\mathfrak{y}}=\mathcal{J}_1\frac{\partial^2\mathbb{w}}{\partial\mathfrak{t}^2},\end{gathered} \tag{18c}$$

$$\begin{gathered}\delta\phi_{\mathfrak{x}}:\ \mathbb{B}_{11}\frac{\partial^2\mathbb{u}}{\partial\mathfrak{x}^2}+\mathbb{B}_{66}\frac{\partial^2\mathbb{u}}{\partial\mathfrak{y}^2}+\frac{\mathcal{A}_{55}\mathbb{u}}{R_1}+\mathbb{B}_{12}\frac{\partial^2\mathbb{v}}{\partial\mathfrak{x}\partial\mathfrak{y}}+\\ \mathbb{B}_{66}\frac{\partial^2\mathbb{v}}{\partial\mathfrak{x}\partial\mathfrak{y}}+\frac{\mathbb{B}_{11}}{R_1}\frac{\partial\mathbb{w}}{\partial\mathfrak{x}}+\mathbb{B}_{12}\frac{\partial\mathbb{w}}{R_2\partial\mathfrak{x}}-\mathcal{A}_{55}\frac{\partial\mathbb{w}}{\partial\mathfrak{x}}+\mathbb{D}_{11}\frac{\partial^2\phi_{\mathfrak{x}}}{\partial\mathfrak{x}^2}+\\ \mathbb{D}_{66}\frac{\partial^2\phi_{\mathfrak{x}}}{\partial\mathfrak{y}^2}-\mathcal{A}_{55}\phi_{\mathfrak{x}}+\mathbb{D}_{12}\frac{\partial^2\phi_{\mathfrak{y}}}{\partial\mathfrak{x}\partial\mathfrak{y}}+\mathbb{D}_{66}\frac{\partial^2\phi_{\mathfrak{y}}}{\partial\mathfrak{x}\partial\mathfrak{y}}=\mathcal{J}_2\frac{\partial^2\mathbb{u}}{\partial\mathfrak{t}^2}+\\ \mathcal{J}_3\frac{\partial^2\phi_{\mathfrak{x}}}{\partial\mathfrak{t}^2},\end{gathered} \tag{18d}$$

$$\begin{gathered}\delta\phi_{\mathfrak{y}}:\ \mathbb{B}_{12}\frac{\partial^2\mathbb{u}}{\partial\mathfrak{x}\partial\mathfrak{y}}+\mathbb{B}_{66}\frac{\partial^2\mathbb{u}}{\partial\mathfrak{x}\partial\mathfrak{y}}+\mathbb{B}_{22}\frac{\partial^2\mathbb{v}}{\partial\mathfrak{y}^2}+\mathbb{B}_{66}\frac{\partial^2\mathbb{v}}{\partial\mathfrak{x}^2}+\\ \frac{\mathcal{A}_{44}\mathbb{v}}{R_2}+\frac{\mathbb{B}_{12}\partial\mathbb{w}}{R_1\partial\mathfrak{y}}+\frac{\mathbb{B}_{22}}{R_2}\frac{\partial\mathbb{w}}{\partial\mathfrak{y}}-\mathcal{A}_{44}\frac{\partial\mathbb{w}}{\partial\mathfrak{y}}+\mathbb{D}_{12}\frac{\partial^2\phi_{\mathfrak{x}}}{\partial\mathfrak{x}\partial\mathfrak{y}}+\\ \mathbb{D}_{66}\frac{\partial^2\phi_{\mathfrak{x}}}{\partial\mathfrak{x}\partial\mathfrak{y}}+\mathbb{D}_{22}\frac{\partial^2\phi_{\mathfrak{y}}}{\partial\mathfrak{y}^2}+\mathbb{D}_{66}\frac{\partial^2\phi_{\mathfrak{y}}}{\partial\mathfrak{x}^2}-\mathcal{A}_{44}\phi_{\mathfrak{y}}=\mathcal{J}_2\frac{\partial^2\mathbb{v}}{\partial\mathfrak{t}^2}+\\ \mathcal{J}_3\frac{\partial^2\phi_{\mathfrak{y}}}{\partial\mathfrak{t}^2}.\end{gathered} \tag{18e}$$

in which

$$(\mathcal{A}_{ij},\mathbb{B}_{ij},\mathbb{D}_{ij})=\int_{-h/2}^{h/2}\quad\mathbb{Q}_{ij}(1,\mathfrak{z},\mathfrak{z}^2)d\mathfrak{z},\ (i,j=1,2,6), \tag{19a}$$

$$\mathcal{A}_{ij}=\int_{-h/2}^{h/2}\quad k_s\mathbb{Q}_{ij}d\mathfrak{z},(i,j=4,5). \tag{19b}$$

where the coefficient of shear correction, k_s, has a value of $5/6$.

4. Solution procedure

The predicted pth derivative associated with a function $\mathcal{F}(\mathfrak{x})$, according to the methods, is:

$$\frac{\partial^p\mathcal{F}(\mathfrak{x})}{\partial\mathfrak{x}^p}=\sum_{j=1}^{N_{\mathfrak{x}}}\mathcal{A}_{ij}^{(p)}\mathcal{F}(\mathfrak{x})\,\mathcal{F}or\ i=1,2,\ldots,N_{\mathfrak{x}} \tag{20}$$

Here, N stands for the discrete points chosen from the solution field. The weighting coefficients for the ith point in the solution domain are represented by $\mathcal{A}_{ij}^{(p)}$, where $j = 1,2,\ldots,N_{\mathfrak{x}}$. This approach transforms a partial differential equation into a system of algebraic equations in order to approximate it. Determining the weighting coefficients is crucial for both the DQ and HDQ approaches, as shown by Eq. (20). The precise procedures needed to determine the weighting coefficients for each method are demonstrated in the examples that follow.

4.1 Differential quadrature method

The recurrence formula of the DQ technique can be used to find the weighting coefficients $\mathcal{A}_{ij}^{(p)}$, which is as follows:

$$\mathcal{A}_{ij}^{(p)} = n\left(\mathcal{A}_{ii}^{(p-1)}\mathcal{A}_{ij}^{(1)} - \frac{\mathcal{A}_{ij}^{(p-1)}}{\mathfrak{x}_i - \mathfrak{x}_j}\right), \quad p = 2,3,\ldots,N_{\mathfrak{x}} - 1 \;\; and \;\; i,j = 1,2,\ldots,N_{\mathfrak{x}}, \tag{21}$$

Herein, $\mathcal{A}_{ij}^{(1)}$ can be determined:

$$\mathcal{A}_{ij}^{(1)} = \frac{M^{(1)}(\mathfrak{x}_i)}{(\mathfrak{x}_i - \mathfrak{x}_j)M^{(1)}(\mathfrak{x}_j)}, i,j = 1,2,\ldots,N_{\mathfrak{x}} \tag{22}$$

The following are the corresponding weighting coefficients when $i = j$:

$$\mathcal{A}_{ii}^{(p)} = -\sum_{j=1, j\neq i}^{N_{\mathfrak{x}}} \mathcal{A}_{ij}^{(p)}, \quad i = 2,3,\ldots,N_{\mathfrak{x}} \;\; and \;\; p = 1,2,\ldots,N_{\mathfrak{x}} - 1 \tag{23}$$

$M^{(1)}$ in Eq. (22), can be expressed as follows:

$$M^{(1)}(\mathfrak{x}_k) = -\sum_{j=1, j\neq k}^{N_{\mathfrak{x}}} (\mathfrak{x}_k - \mathfrak{x}_j), \quad \mathcal{F}or \;\; k = 1,2,3,\ldots,N_{\mathfrak{x}}. \tag{24}$$

4.2 Harmonic Differential Quadrature Method (HDQM)

The formula below provides the proper weights for the first-order derivatives $\mathcal{A}_{ij}^{(1)}$ for $i \neq j$:

$$\mathcal{A}_{ij}^{(1)} = \frac{\pi P(\mathfrak{x}_i)}{2P(\mathfrak{x}_j)\, sin[(\mathfrak{x}_i - \mathfrak{x}_j)/2\pi]}, \;\; i,j = 1,2,\ldots,N_{\mathfrak{x}}, \tag{25}$$

where

$$P(\mathfrak{x}_i) = -\sum_{j=1, j\neq i}^{N_{\mathfrak{x}}} sin\left(\frac{\pi(\mathfrak{x}_i - \mathfrak{x}_j)}{2}\right), \mathcal{F}or \; j = 1,2,3,\ldots,N_{\mathfrak{x}}. \tag{26}$$

The weights of the first order derivatives $\mathcal{A}_{ij}^{(1)}$ for $i = j$ are as follows:

$$\mathcal{A}_{ii}^{(1)} = -\sum_{j=1, j\neq i}^{N_{\mathfrak{x}}} \mathcal{A}_{ij}^{(1)}, \mathcal{F}or \;\; i = 1,2,3,\ldots,N_{\mathfrak{x}}. \tag{27}$$

For $i \neq j$, the second-order derivative weights $\mathcal{A}_{ij}^{(2)}$ can be computed as follows:

$$\mathcal{A}_{ij}^{(2)} = \mathcal{A}_{ij}^{(1)}\left(2\mathcal{A}_{ij}^{(1)} - \pi c\mathfrak{t}g\left(\frac{\mathfrak{x}_i - \mathfrak{x}_j}{2} \times \pi\right)\right), i,j = 1,2,3,\ldots,N_{\mathfrak{x}} \tag{28}$$

The weighting factors for the derivatives $\mathcal{A}_{ij}^{(2)}$ for $i = j$ are as follows:

$$\mathcal{A}_{ii}^{(2)} = -\sum_{j=1, j\neq i}^{N_{\mathfrak{x}}} \mathcal{A}_{ij}^{(2)}, \mathcal{F}or \;\; i = 1,2,3,\ldots,N_{\mathfrak{x}} \tag{29}$$

4.3 Two-dimensional approximation

It is simple to adapt the HDQ and DQ techniques, which were first created for one-dimensional issues, to three-dimensional approximations. The following are the formulas for estimating a two-dimensional unknown function $\mathcal{F}\,(\mathfrak{x},\mathfrak{y})$:

$$\left.\frac{\partial\mathcal{F}}{\partial\mathfrak{x}}\right|_{\mathfrak{x}=\mathfrak{x}_i,\mathfrak{y}=\mathfrak{y}_j} = \textstyle\sum_{p=1}^{N_{\mathfrak{x}}}\sum_{k=1}^{N_{\mathfrak{y}}} \mathcal{A}_{ip}^{\mathfrak{x}}\, \mathscr{i}_{pk}^{\mathfrak{y}} \mathcal{F}_{kj}, \tag{30a}$$

$$\left.\frac{\partial\mathcal{F}}{\partial\mathfrak{y}}\right|_{\mathfrak{x}=\mathfrak{x}_i,\mathfrak{y}=\mathfrak{y}_j} = \textstyle\sum_{p=1}^{N_{\mathfrak{x}}}\sum_{k=1}^{N_{\mathfrak{y}}} \mathscr{i}_{ip}^{\mathfrak{x}}\, \mathcal{A}_{pk}^{\mathfrak{y}} \mathcal{F}_{kj}, \tag{30b}$$

$$\frac{\partial}{\partial\mathfrak{x}}\left(\left.\frac{\partial\mathcal{F}}{\partial\mathfrak{y}}\right|_{\mathfrak{x}=\mathfrak{x}_i,\mathfrak{y}=\mathfrak{y}_j}\right) = \textstyle\sum_{p=1}^{N_{\mathfrak{x}}}\sum_{k=1}^{N_{\mathfrak{y}}} \mathcal{A}_{ip}^{\mathfrak{x}}\, \mathcal{A}_{pk}^{\mathfrak{y}} \mathcal{F}_{kj}, \tag{30c}$$

$$\left.\frac{\partial^2\mathcal{F}}{\partial\mathfrak{x}^2}\right|_{\mathfrak{x}=\mathfrak{x}_i,\mathfrak{y}=\mathfrak{y}_j} = \textstyle\sum_{p=1}^{N_{\mathfrak{x}}}\sum_{k=1}^{N_{\mathfrak{y}}} \mathbb{B}_{ip}^{\mathfrak{x}}\, \mathscr{i}_{pk}^{\mathfrak{y}} \mathcal{F}_{kj}, \tag{30d}$$

$$\left.\frac{\partial^2\mathcal{F}}{\partial\mathfrak{y}^2}\right|_{\mathfrak{x}=\mathfrak{x}_i,\mathfrak{y}=\mathfrak{y}_j} = \textstyle\sum_{p=1}^{N_{\mathfrak{x}}}\sum_{k=1}^{N_{\mathfrak{y}}} \mathscr{i}_{ip}^{\mathfrak{x}}\, \mathbb{B}_{pk}^{\mathfrak{y}} \mathcal{F}_{kj}. \tag{30e}$$

Here, the weighting coefficients for the pth partial derivatives of the function at the point (i,j) with respect to the $\mathfrak{x}$ and $\mathfrak{y}$ axes are denoted by $\mathcal{A}_{ip}^{\mathfrak{x}}$, $\mathcal{A}_{pk}^{\mathfrak{y}}$, $\mathbb{B}_{ip}^{\mathfrak{x}}$, and $\mathbb{B}_{pk}^{\mathfrak{y}}$. The total number of discrete points chosen in different directions is shown by the symbols $N_{\mathfrak{x}}$ and $N_{\mathfrak{y}}$. The identity matrix is denoted by the parameters $\mathscr{i}_{ip}^{\mathfrak{x}}$, $\mathscr{i}_{pk}^{\mathfrak{y}}$, $\mathscr{i}_{ip}^{\mathfrak{x}}$, and $\mathscr{i}_{pk}^{\mathfrak{y}}$. Likewise, the coordinates of the grid points $(\mathfrak{x}_i, \mathfrak{y}_j)$ on the reference surface can be found using the Chebyshev–Gauss–Lobatto grid distribution:

$$\mathfrak{x}_i = \tfrac{a}{2}\left(1 - cos\left(\tfrac{(i-1)}{(N_{\mathfrak{x}}-1)}\pi\right)\right) i = 1,2,3,\ldots,N_{\mathfrak{x}}, \tag{31a}$$

$$\mathfrak{y}_j = \tfrac{b}{2}\left(1 - cos\left(\tfrac{(j-1)}{(N_{\mathfrak{y}}-1)}\pi\right)\right) j = 1,2,3,\ldots,N_{\mathfrak{y}}, \tag{31b}$$

The variable separation approach yields the displacement field of the functionally graded composite nanostructured thick shell, which is stated as follows:

$$\mathbb{u}(\mathfrak{x},\mathfrak{y},\mathrm{t}) = \mathbb{u}_0(\mathfrak{x},\mathfrak{y})e^{i\omega\mathrm{t}}, \tag{32a}$$

$$\mathbb{v}(\mathfrak{x},\mathfrak{y},\mathrm{t}) = \mathbb{v}_0(\mathfrak{x},\mathfrak{y})e^{i\omega\mathrm{t}}, \tag{32b}$$

$$\mathbb{w}(\mathfrak{x},\mathfrak{y},\mathrm{t}) = \mathbb{w}_0(\mathfrak{x},\mathfrak{y})e^{i\omega\mathrm{t}}, \tag{32c}$$

$$\not{f}_{\mathfrak{x}}(\mathfrak{x},\mathfrak{y},\mathfrak{t}) = \not{f}_{\mathfrak{x}0}(\mathfrak{x},\mathfrak{y})e^{i\omega\mathfrak{t}}, \tag{32d}$$

$$\not{f}_{\mathfrak{y}}(\mathfrak{x},\mathfrak{y},\mathfrak{t}) = \not{f}_{\mathfrak{y}0}(\mathfrak{x},\mathfrak{y})e^{i\omega\mathfrak{t}}. \tag{32e}$$

where J is equal to 0, 1, 2, 3. The imaginary unit is also denoted by i ($i=\sqrt{-1}$). The following results from replacing Eqs. (32a)-(32e) in the governing equations:

$$(-\omega^2[\boldsymbol{\mathfrak{M}}] + [\mathbb{K}])\{\bar{\mathbb{X}}\} = 0, \tag{33a}$$

$$\{\bar{\mathbb{X}}\} = \{\mathbb{u}_0 \ \ \mathbb{v}_0 \ \ \mathbb{w}_0 \ \ \not{f}_{\mathfrak{x}} \ \ \not{f}_{\mathfrak{y}}\}^T. \tag{33b}$$

'$\boldsymbol{\mathfrak{M}}$', and '$\mathbb{K}$' stand for the mass and stiffness matrices, respectively, in the provided equations. The system's natural frequencies are given by the solution to Eq. (33a). The following formula can be used to get the dimensionless frequency:

$$\omega^* = 10 \times \omega a\sqrt{\rho_m/E_m} \tag{34}$$

5. Results and discussion

5.1 Validation

Table 1 shows the comparison of natural frequencies of shallow shell structures between the outcomes of this study and a number of reference works, which is important for validating the findings of the computational model used in this project, specifically with doubly curved panels subjected to aerodynamic loads. Each of the natural frequencies and mode numbers listed on the table shows the picometer natural frequencies computed in both this study and the preliminary studies (Refs. (Chern and Chao 2000), (Fan and Luah 1995), (Hosseini-Hashemi and Fadaee 2011), and (Khare *et al*. 2004)). The frequencies listed are some arbitrary number of the first matching natural frequencies that are useful for the structural dynamics and stability response of shallow shell structures. The comparison verifies the accuracy of the computational method's predictions of vibrational characteristics with nanocomposite reinforcement of shallow shells as applicable to a reliability demonstration. The small variation in the natural frequencies was reported to be reflective of the variations that are due to the modeling frameworks, material variation, and/or boundary condition differences present in each modeling study. Comparisons of this nature are necessary to ensure the method is used effectively and reliably for amenable stability analysis and further optimization issues concerning nanocomposite shallow shell structures. This comparison establishes credibility for the thickness-dependent shear deformation theory and HDQM for recognizing the dynamic response of such engineering structures.

5.2 Parametric results

Fig. 2 presents the time histories of kinetic energy (KE) and potential energy (PE) in a nanocomposite-reinforced panel under airflow at a range of velocities: each graph presents KE and PE response to airflow velocity V_{air}=30 (left) and V_{air}=60m/s (right) over time, here plotted as 8 seconds, and demonstrate the response of the panel to aerodynamic loading and modifications of motion over time. The two energy forms fluctuate and react to the aerodynamic loading while the potential energy fluctuations are proportional to the amplitude of the kinetic energy fluctuations. Although kinetic energy and potential energy respond to changes in matter, the potential energy is more than likely a more dominant factor intuitively as the

Table 1 A comparison between shallow shell natural frequencies and those found in the literature

Mode numbers	Ref. (Chern and Chao 2000)	Ref. (Fan and Luah 1995)	Ref. (Hosseini-Hashemi and Fadaee 2011)	Ref. (Khare *et al*. 2004)	Present
(1, 1)	0.52543	0.53263	0.52830	0.50223	0.53125
(1, 2)	0.58420	0.59041	0.58853	0.56276	0.59215
(2, 1)	0.58427	0.59080	0.58853	0.56277	0.58126
(2, 2)	0.67676	0.68486	0.68232	0.65788	0.68480

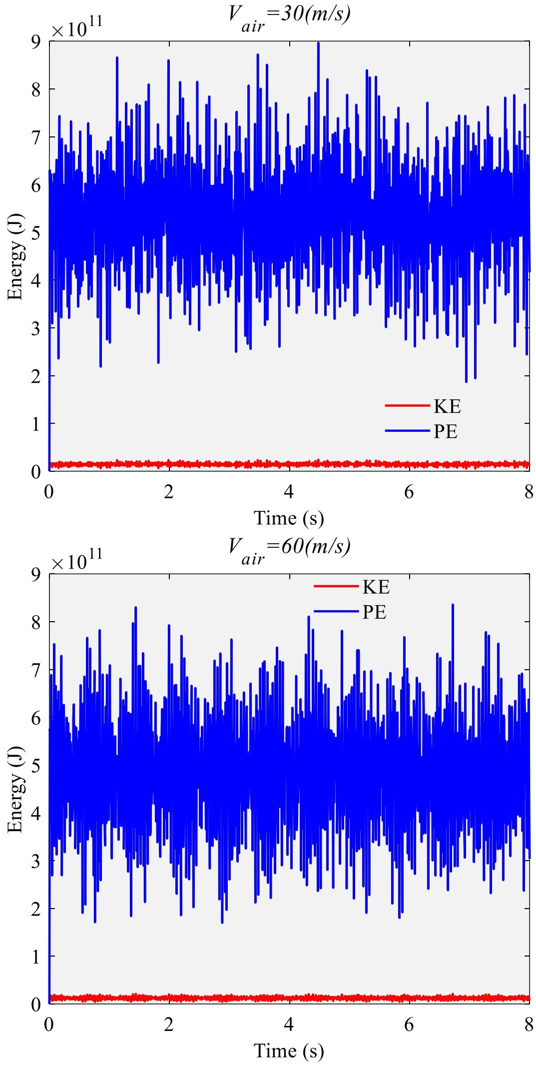

Fig. 2 The time histories of kinetic energy and potential energy in a nanocomposite-reinforced panel under airflow at a range of velocities

potential energy in a nanocomposite panel is more closely driven and reliant on composite density and moment arms of terms within the panel. The fluctuation cycles of these two types of energy depicts important scaffolding for determining aspects of dynamic stability in the nanocomposite panel. The change in energy between the two situations is very visible, where having a larger airflow speed (60 m/s) results in larger oscillations in both KE and PE leading to a larger structural response as a result of the aerodynamic force. A better understanding of the distribution of energy and how that dissipates or loses energy will help any analysis with respect to stability. The ratio of kinetic energy to potential energy is informative in regards to how much damping takes place within the system and what energy the structure could potentially absorb. This figure demonstrates our theory that higher airflow speeds results in a greater dynamic response which ultimately means the potential for instability should they not be dealt with properly. Understanding these dynamics will be useful to us in optimizing nanocomposite-reinforced panels since they can help us make changes to either the geometry of the panel or the material properties of the panel to improve their performance at varying airflow speeds.

Fig. 3 depicts the influence of the carbon nanotube volume fraction on the dimensionless natural frequency of the panel reinforced with nanocomposite for different airflow speeds. The x-axis displays the airflow velocity in m/s, while the y-axis provides the dimensionless frequency. There are four values of CNT volume fractions that were analyzed: $W_{CNT} = 0\%, 0.5\%, 1\%$, and 1.5% each represented with different line styles. The results show that the increasing concentration of the CNT volume fraction reduces the natural frequency of the panel. This characteristic indicates that it is important to achieve an optimum loading of CNT in the reinforcement to avoid compromising structural stiffness against dynamic behavior. This point was important for ensuring that nanocomposite panels remain stable under aerodynamics loads with tester airflow conditions.

Fig. 4 explores the effect of CNT distribution types for all the same airflow velocities on the dimensionless natural frequency of the nanocomposite-reinforced panels. The x-axis shows airflow velocity and the y-axis shows dimensionless frequency values. The different CNT distribution types for the panels are presented in four different line styles along the vertical axis, including CNT-X, CNT-O, CNT-V, and CNT-UD. The evidence suggests that different CNT distributions behave dynamically in different ways based on experimental distribution type. Specifically, the CNT-X distribution provides the highest dimensionless frequency, followed by CNT-O, CNT-V, and CNT-UD. The different dimensionless frequency values illustrate the significance of choosing an adequate CNT distribution to enhance the vibrational characteristics and stability of nanocomposite panels in aerodynamic loads.

Fig. 5 investigates the influence of panel curvature on the dimensionless natural frequency of the nanocomposite-reinforced panel while varying curvature ratios. The x-axis represents flow velocity, and the y-axis is the dimensionless frequency. The curves represent the various values of the

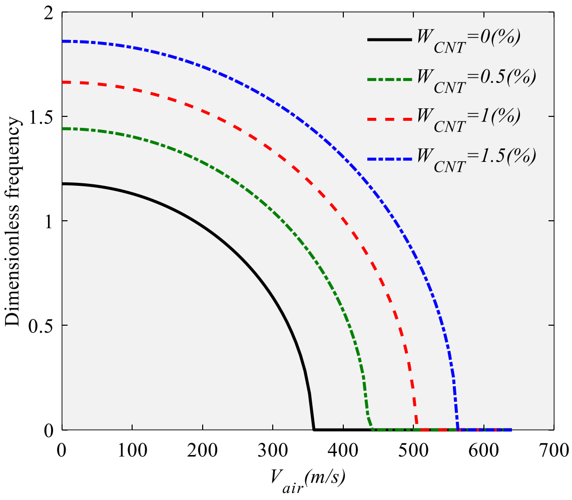

Fig. 3 The influence of the carbon nanotube volume fraction on the dimensionless natural frequency of the panel reinforced with nanocomposite for different airflow speeds

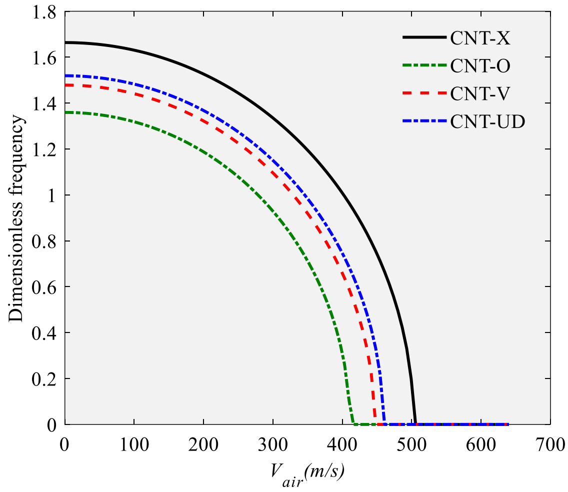

Fig. 4 The effect of CNT distribution types for all the same airflow velocities on the dimensionless natural frequency of the nanocomposite-reinforced panels

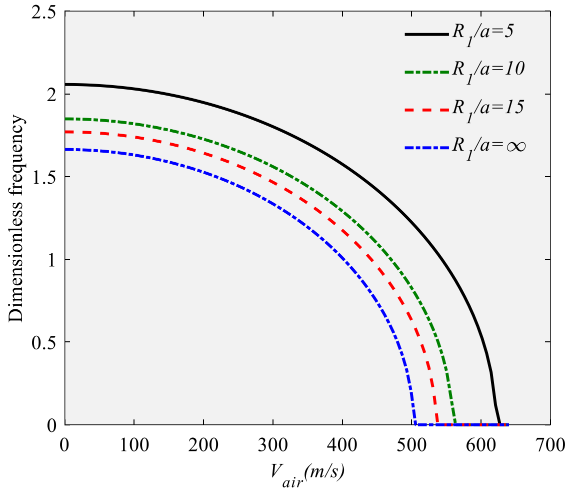

Fig. 5 The influence of panel curvature on the dimensionless natural frequency of the nanocomposite-reinforced panel while varying curvature ratios

ratio $R_1/a = 5, 10, 15$, and ∞, which are represented by different line styles. The results suggest that, as the panel curvature increases (lower R_1/a values), the natural frequency also increases. This means that more curved panels present less sensitivity to aerodynamic forces and exhibit a greater level of stability at higher velocities. The effect of curvature is paramount to panel design application, as it provides information on the dynamics of the panel when undergoing aerodynamic loading.

Fig. 6 examines the influence of the ratio R_2/R_1 on the dimensionless frequency, with differing ratio values. Again, the x-axis represents the airflow velocity and the y-axis represents the dimensionless frequency. The ratio R_2/R_1 has values of $-1, 1, 5$, and infinity, with each represented by a different line style. In the results, as the curvature ratio R_2/R_1 is increased, the dimensionless frequency decreased, indicating that higher values of R_2/R_1 lower the panel's structural stiffness. The implications of curvature in the optimization process show where taking time on which geometry to use for the panel could improve performance under aerodynamic loading.

Fig. 7 illustrates the relationship between dimensionless frequency and airflow velocity at four distinct angles of airflow. The figure shows that all four angles of airflow are plotted with different line styles. The data shows that as airflow angle increases, natural frequency decreases for any given airflow velocity. The effect could suggest that the natural frequency is decreasing because the angle of attack results in the panel being subjected to higher aerodynamic forces, altering the behavior of the system and the vibrational response of this system. The graph illustrates the significance of airflow angle and its attendant effects on the structural dynamics and stability of nanocomposite-reinforced panels subjected to aerodynamic loading. The results indicate that careful consideration of airflow direction and its effect on the performance of engineering structures need to be addressed, particularly with regards to aerodynamic applications.

Fig. 8 looks at the impact of carbon nanotube volume fraction on the dimensionless natural frequency of the nano-composite-reinforced panel with respect to the airflow angle. The x-axis is the airflow angle, and the y-axis is the dimensionless frequency. CNT volume fractions of 0%, 0.5%, 1.0%, and 1.5% are evaluated with different line styles. The results indicate a decrease in natural frequency as the CNT volume fraction increases - primarily at higher airflow angles. This intuitively reinforces that with a higher CNT content, the stiffness of the panel is diminished while its flexibility is increased under dynamic loading conditions. This figure demonstrates the importance of both CNT content and airflow angle when working to optimize the dynamic properties of nano-composite panels with respect to potential engineering applications.

Fig. 9 represents the impact of CNT distribution on the respective dimensionless frequency of the nanocomposite-reinforced panel under various airflow angles. In this graph, four different CNL distributions are demonstrated: CNT-X, CNT-O, CNT-V, and CNT-UD, which are identified with their respective line styles. The effectiveness of each CNT distribution was similarly conclusive once again. Indicating

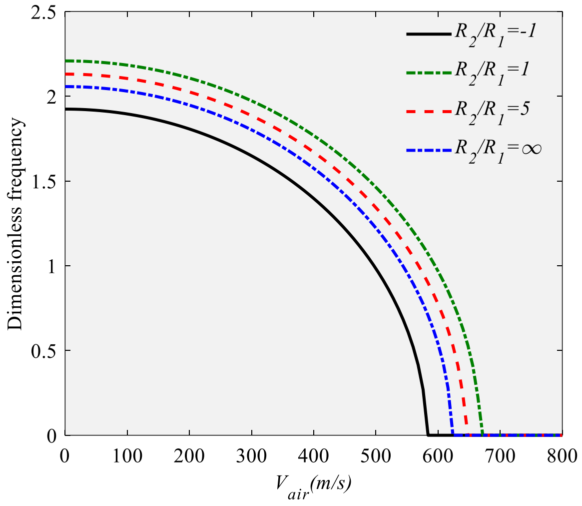

Fig. 6 The influence of the ratio $\boldsymbol{R_2/R_1}$ on the dimensionless frequency, with differing ratio values

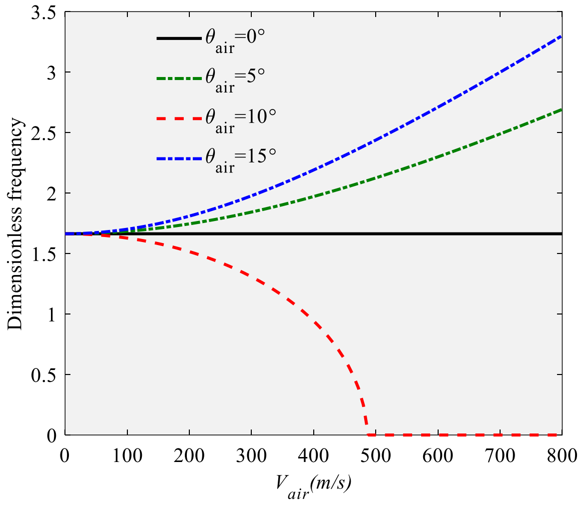

Fig. 7 The relationship between dimensionless frequency and airflow velocity at four distinct angles of airflow

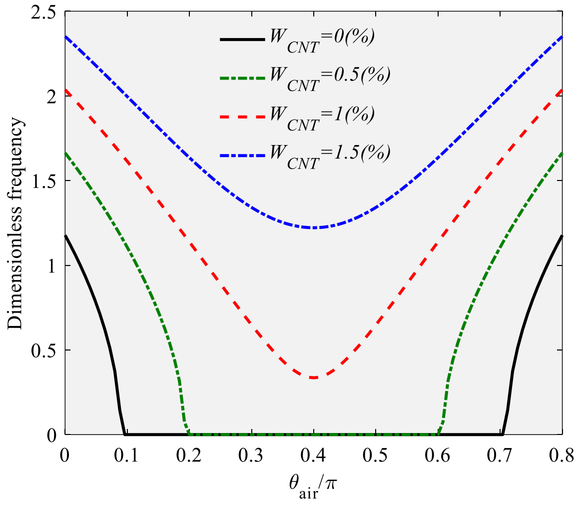

Fig. 8 The impact of carbon nanotube volume fraction on the dimensionless natural frequency of the nano composite-reinforced panel with respect to the airflow angle

that CNT-X distribution yielded the highest natural frequency, CNT-O was a precinct lower, followed by CNT-V, and lastly CNT-UD. For example, the airflow angle depicted along the x-axis affected the vibrational behaviour of the panels studied. In this three-dimensional parametric construct, as the airflow angle increased, so did the effect on natural frequency reduction. Throughout all four CNT distributions, a decrease in natural frequency can be witnessed with the increase in angle, however, CNT-X maintains the greatest frequency limit. This study indicates the significance of choosing the proper CNT distribution to adhere to the structural performance of the material examined, especially in regards to varying aerodynamic behaviour and conditions.

Fig. 10 illustrates the curvature effect on dimensionless frequency with varying curvature ratios. The x-axis is airflow angle, while the y-axis is dimensionless frequency. Each curve is representative of a given curvature ratio: 5, 10, 15, and infinity. The data show that at greater curvature ratios that the natural frequency is also greater, but particularly at larger airflow angles. This impulsively implies that greater curvature panels are considerably more rigid and less affected by aerodynamic forces, signifying they perform better at greater airflow angles. This figure illustrates how the use of geometric design can significantly affect aspects of structural performance, but more importantly, why geometric design is vital to help achieve performance optimized from an operational perspective, in the design of aerodynamically loaded nanocomposite panels, where curvature is a major contributor to the controllability of normal vibratory response while achieving integrity of structure.

Fig. 11 provides the stability investigation of nanocomposite-reinforced panels, considering the relationship between airflow angle and non-dimensional frequency. There are four different curves based on the curvature factor ratio. The U-shape can be seen in that the non-dimensional frequency decreases as the airflow angle increases, and it reaches a minimum frequency around 0.40 on the x-axis. Although the curvature ratio varies, the behavior of frequency varies, indicating that the stability of a panel subjected to wind may be a function of its shape. Therefore, the figure reveals further information about how varying panel curvature affects the dynamic acquiescence frequency to different airflow characteristics, and illustrates the interdependencies to optimize panel geometry for wind loading applications in practice.

Fig. 12 studies the impact of CNT weight fractions on the dimensional frequency of a panel reinforced with a nanocomposite, and subject to airflow conditions. The x-axis is the radius ratio and the total length of the panel, with R_1 representing the curvature factor in the x direction. The y-axis is the dimensional frequency, showing how the structural frequency is influenced with respect to CNT weight fraction and radius ratio. Four curves are shown, which correspond to the CNT content for that configuration. Dimensional frequency decreased with the increase in CNT weight fraction, as the panels became more flexible in the structure. This would suggest that the dynamic behavior is significantly impacted by the CNT reinforcement, and that

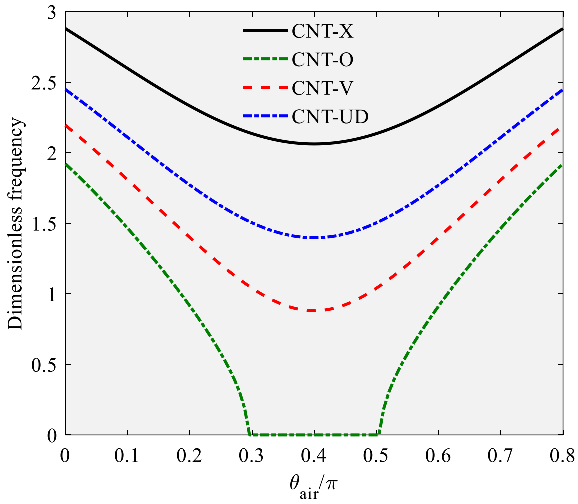

Fig. 9 The impact of CNT distribution on the respective dimensionless frequency of the nanocomposite-reinforced panel under various airflow angles

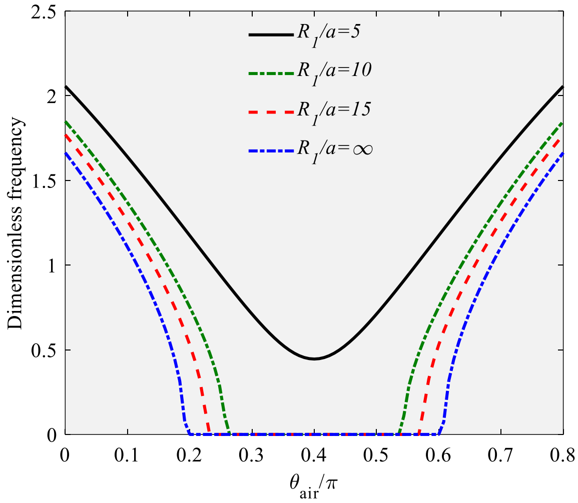

Fig. 10 The curvature effect on dimensionless frequency with varying curvature ratios

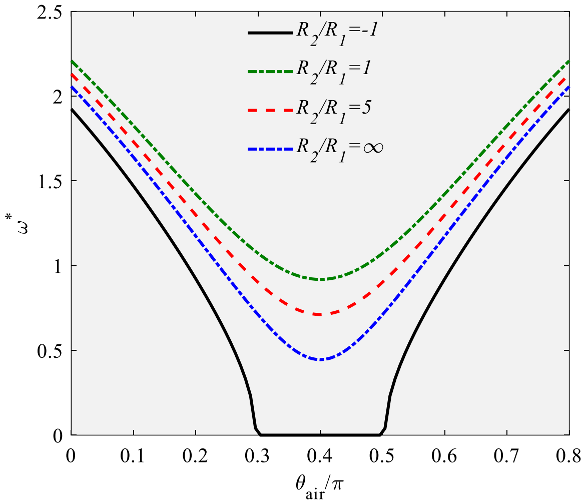

Fig. 11 The stability investigation of nanocomposite-reinforced panels, considering the relationship between airflow angle and non-dimensional frequency

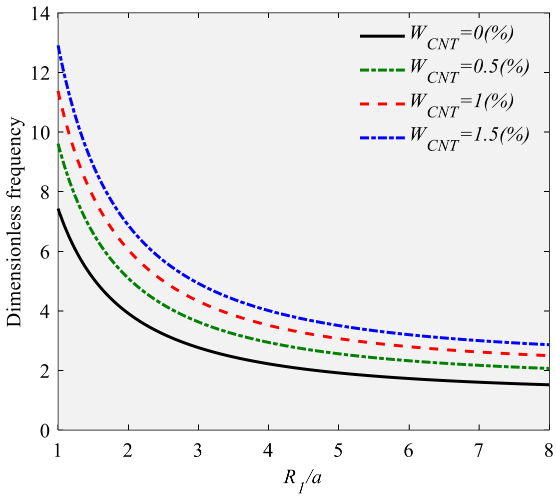

Fig. 12 The impact of CNT weight fractions on the dimensional frequency of a panel reinforced with a nanocomposite, and subject to airflow conditions

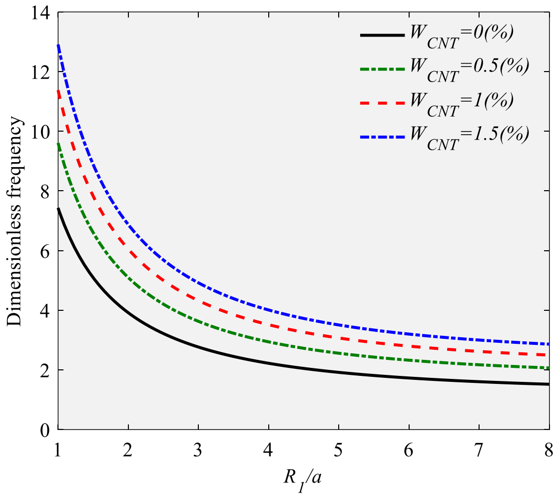

Fig. 13 The dimensional frequency of nanocomposite-reinforced panels as a function of radius ratio, depending on the weight fractions of CNT

the mechanical properties of panels can therefore be tailored for optimized aerodynamic performance.

Fig. 13 explores the dimensional frequency of nanocomposite-reinforced panels as a function of radius ratio, depending on the weight fractions of CNT. This graph also discusses stability criteria with regard to airflow conditions. In this graph, the x-axis represents the radius ratio and the y-axis represents the appropriate dimensional frequency. The curves are marked based on four different values of the weight fraction of CNT. These can be linked to the volume fraction of CNTs embedded in the matrix. Similar to the previous results outlined in Figure 3, the frequency for the lower CNT content panels decreases as the CNT content increases. There is a clear indication of greater flexibility, decreased internal stiffness or elastic modulus, and therefore can expect a great overall deflection in the panels influenced by the aerodynamic forces acting on the panel. Overall, this figure is useful for designers who are interested in evaluating the use of CNT-reinforced panels, where transition from modeling materials to evaluating the vibrational behavior of reinforced panels, potentially with tailored CNT fractions, occurs during actual mechanical capacity. This emphasizes a potential for optimizing a specific weight fraction of CNT materials to achieve desired mechanical properties and stability.

6. Conclusions

In conclusion, this study has investigated the stability and optimization management of nanocomposite-reinforced doubly curved panels under different airflow conditions involving airflow speed and airflow angle. Through the employment of a thickness-dependent shear deformation theory, the research has taken into account the complexities of panel behavior under aerodynamic forces, more specifically, that of structural stability and material performance. The research utilized the harmonic differential quadrature method to provide a useful numerical approach to solve the governing equations obtained in this study, and allowed for meaningful data about the behavior of the dynamic response of the system to be obtained. The sensitivity analysis has also contributed to our understanding of the role of carbon nanotube reinforcement in improving the mechanical properties of nanocomposites, specifically, the rule of mixtures approach worked quite well to characterize the effective mechanical properties of the composite material. In addition, the incorporation of Hooke's law for elastic materials and Hamilton's principle led us to derive the governing equations that describe the system's characteristics under the effects of aerodynamic loading. The optimization framework presented here had a narrow focus on obtaining the optimal solution that derived the maximum stability of the panel by modifying both geometric and material properties, and which provided inherent improvements to the performance capabilities of the doubly curved panels. Finally, in this study, airflow characteristics, specifically speed and angle, had an effect on the structural response of the panels, as had been anticipated by the authors. The analysis found that, as with only the airflow speed increasing, increasing the angle in addition created directional forces of the aero loading.

Acknowledgement

The research is funded by Zarqa University.

Funding

The research is funded by Zarqa University.

References

Al-Houri, S., Al-Osta, M.A., Gawah, Q., Bourada, F., Tounsi, A., Al-Dulaijan, S.U. and Tounsi, A. (2024), "Wave propagation analysis of composite beams reinforced with nonlinear fg-cnt distributions supported on kerr elastic foundation utilizing an improved integral first-order shear deformation theory", *Geomech. Eng.*, **39**(5), 483. https://doi.org/10.12989/gae.2024.39.5.483

Alsubaie, A.M., Al-Osta, M.A., Alfaqih, I., Tounsi, A., Chikh, A., Mudhaffar, I.M., Al-Dulaijan, S.U. and Tahir, S. (2024), "Influences of porosity distributions on bending and buckling behaviour of functionally graded carbon nanotube-reinforced composite beam", *Comput. Concr.*, **34**(2), 179-193. https://doi.org/10.12989/cac.2024.34.2.179

Arshid, E., Ghorbani, M.A., Momeni Nia, M.J., Civalek, Ö. and Kumar, A. (2023), "Thermo-elastic buckling behaviors of advanced fluid-infiltrated porous shells integrated with gpls-reinforced nanocomposite patches", *Mech. Adv. Mater. Struct.*, 1-17. https://doi.org/10.1080/15376494.2023.2251015

Avcar, M., Hadji, L. and Civalek, O. (2023), "The influence of non-linear carbon nanotube reinforcement on the natural frequencies of composite beams", *Adv. Nano Res.*, **14**(5), 421-433. https://doi.org/10.12989/anr.2023.14.5.421

Babaei, H., Zavari, S., Kaveh, A., Arshid, E. and Civalek, Ö. (2024), "Dynamic response of advanced lightweight porous plates integrated with nanocomposite face sheets resting on elastic substrate", *Int. J. Struct. Stabil. Dyn.*, **25**(12), 2550132. https://doi.org/10.1142/S0219455425501329

Bousmaha, K., Belalia, S.A., Chorfi, S.M., Tounsi, A., Al-Osta, M.A. and Alluqmani, A.E. (2025), "On the dynamic behavior of plates made of porous advanced materials reinforced with carbon nanotubes using ap-version of finite element method", *Mech. Based Des. Struct.*, 1-30. https://doi.org/10.1080/15397734.2025.2534679

Boutaleb, S., Boulal, A., Zidour, M., Al-Osta, M.A., Tounsi, A., Tounsi, A., Salem, M.A. and Khedher, K.M. (2024), "On the buckling response of functionally graded carbon nanotube-reinforced composite imperfect beams", *Periodica Polytechnica Civil Eng.*, **68**(4), 1052-1063. https://doi.org/10.3311/PPci.23825

Chern, Y.C. and Chao, C. (2000), "Comparison of natural frequencies of laminates by 3-d theory, part ii: curved panels", *J. Sound Vib.*, **230**(5), 1009-1030. https://doi.org/10.1006/jsvi.1999.2454

Davoise, L.V., Capilla, R.P. and Díez-Pascual, A.M. (2023), "Optical properties of polyaniline/modified graphene oxide nanocomposites", *Mater. Today Commun.*, 106733. https://doi.org/10.1016/j.mtcomm.2023.106733

Ebrahimi, F. and Salari, E. (2018), "Effect of non-uniform temperature distributions on nonlocal vibration and buckling of inhomogeneous size-dependent beams", *Adv. Nano Res.*, **6**(4), 377. https://doi.org/10.12989/anr.2018.6.4.377

Fan, S. and Luah, M. (1995), "Free vibration analysis of arbitrary thin shell structures by using spline finite element", *J. Sound Vib.*, **179**(5), 763-776. https://doi.org/10.1006/jsvi.1995.0051

Forooghi, A., Fallahi, N., Alibeigloo, A., Forooghi, H. and Rezaey, S. (2023), "Static and thermal instability analysis of embedded functionally graded carbon nanotube-reinforced composite plates based on hsdt via gdqm and validated modeling by neural network", *Mech. Based Des. Struct.*, **51**(12), 7149-7182. https://doi.org/10.1080/15397734.2022.2094407

Gawah, Q., Abdullah, M.A., Al-Osta, M.A., Bourada, F., Tounsi, A., Tounsi, A. and Yaylaci, M. (2025), "Free vibration analysis of nonlinearly dispersed fg-cntrc beams on kerr substrate using an improved fsdt", *Struct. Eng. Mech.*, **93**(6), 475-493. https://doi.org/10.12989/sem.2025.93.6.475

Hoang, V.N.V. and Thanh, P.T. (2024), "Nonlinear dynamics of fluid-filled nanocomposite cylindrical shells surrounded by non-uniform kerr elastic substrates", *Int. J. Struct. Stabil. Dyn.*, 2550133. https://doi.org/10.1142/S0219455425501330

Hosseini-Hashemi, S. and Fadaee, M. (2011), "On the free vibration of moderately thick spherical shell panel—a new exact closed-form procedure", *J. Sound Vib.*, **330**(17), 4352-4367. https://doi.org/10.1016/j.jsv.2011.04.011

Jayakumari, B.Y., Swaminathan, E.N. and Partheeban, P. (2024), "Sustainable construction material using nanosilica and multi-walled carbon nanotubes in cement concrete", *Adv. Nano Res.*, **16**(5), 459-472. https://doi.org/10.12989/.2024.16.5.459

Khare, R.K., Kant, T. and Garg, A.K. (2004), "Free vibration of composite and sandwich laminates with a higher-order facet shell element", *Compos. Struct.*, **65**(3-4), 405-418. https://doi.org/10.1016/j.compstruct.2003.12.003

Li, J. and Liu, J. (2025), "Nonlinear optimized pid vibration control of thermal-dependent fg composite porous plates reinforced by agglomerated cnts", *Int. J. Struct. Stabil. Dyn.*, **25**(4), 2550034. https://doi.org/10.1142/S0219455425500348

Liu, W., Deng, L., Cai, Z., Li, D. and Rahimi, A. (2021), "Impact of in-plane follower force on the frequency response of the hybrid angle-ply laminated system via dynamic simulation and generalized differential quadrature framework", *Eng. Comput.*, 1-18. https://doi.org/10.1007/s00366-020-01215-4

Lu, S., Xue, N., Ma, W., Song, X. and Jiang, X. (2025), "Linear and nonlinear dynamics responses of an axially moving laminated composite plate-reinforced with graphene nanoplatelets", *Int. J. Struct. Stabil. Dyn.*, **25**(4), 2550036. https://doi.org/10.1142/S0219455425500361

Mahinzare, M., Rastgoo, A. and Ebrahimi, F. (2024), "On nonlinear vibration of piezo-electrically multiscale hybrid nanocomposite sandwich plate including an auxetic core based on hsdt", *Int. J. Struct. Stabil. Dyn.*, **24**(5), 2450069. https://doi.org/10.1142/S021945542450069X

Nguyen, N.V., Tran, K.Q., Do, D.T.T., Thai, C.H., Żur, K.K. and Nguyen-Xuan, H. (2024), "An isogeometric analysis of solar panels with a bio-inspired substrate", *Eng. Anal. Bound. Elem.*, **166**, 105854. https://doi.org/10.1016/j.enganabound.2024.105854

Rashvand, K., Alibeigloo, A. and Safarpour, M. (2022), "Free vibration and instability analysis of a viscoelastic micro-shell conveying viscous fluid based on modified couple stress theory in thermal environment", *Mech. Based Des. Struct.*, **50**(4), 1198-1236. https://doi.org/10.1080/15397734.2020.1745079

Reddy, J.N. (2003), *Mechanics of Laminated Composite Plates and Shells: Theory and Analysis,* CRC press. https://doi.org/10.1201/b12409

Safaei, B., Sahmani, S. and Tofighi Asl, H. (2023), "Quasi-3d nonlinear flexural response of isogeometric functionally graded cnt-reinforced plates with various shapes with variable thicknesses", *Mech. Based Des. Struct.*, **51**(5), 2957-2981. https://doi.org/10.1080/15397734.2021.1999264

Safarpour, M. and Alibeigloo, A. (2021), "Elasticity solution for bending and frequency behavior of sandwich cylindrical shell with fg-cntrc face-sheets and polymer core under initial stresses", *Int. J. Appl. Mech.*, **13**(2), 2150020. https://doi.org/10.1142/S1758825121500204

Shen, X., Li, T., Xu, L., Kiarasi, F., Babaei, M. and Asemi, K. (2024), "Free vibration analysis of fg porous spherical cap reinforced by graphene platelet resting on winkler foundation", *Adv. Nano Res.*, **16**(1), 11-26. https://doi.org/10.12989/anr.2024.16.1.011

Tounsi, A., Belabed, Z., Bounouara, F., Balubaid, M., Mahmoud, S., Bousahla, A.A. and Tounsi, A. (2024), "A finite element approach for forced dynamical responses of porous fg nanocomposite beams resting on viscoelastic foundations", *Int. J. Struct. Stabil. Dyn.*, 2650078. https://doi.org/10.1142/S0219455426500781

Viola, E., Tornabene, F. and Fantuzzi, N. (2013), "Static analysis of completely doubly-curved laminated shells and panels using general higher-order shear deformation theories", *Compos. Struct.*, **101**, 59-93. https://doi.org/10.1016/j.compstruct.2013.01.002

Xia, L., Wang, R., Chen, G., Asemi, K. and Tounsi, A. (2023), "The finite element method for dynamics of fg porous truncated conical panels reinforced with graphene platelets based on the 3-d elasticity", *Adv. Nano Res.*, **14**(4), 375-389. https://doi.org/10.12989/.2023.14.4.375

Youzera, H., Meftah, S.A., Tounsi, A., Salem, M.A., Khedher, K.M. and Yaylacı, M. (2025a), "Nonlinear forced vibration analysis of fg-cntrc sandwich beams with viscoelastic core under various boundary conditions", *Mech. Adv. Mater. Struct.*, 1-10. https://doi.org/10.1080/15376494.2025.2473691

Youzera, H., Meftah, S.A., Tounsi, A., Salem, M.A., Khedher, K. M. and Yaylacı, M. (2025b), "Free vibration analysis of sandwich cylindrical shells with functionally graded carbon nanotube-reinforced composite face sheets using the differential quadrature (dq) method", *Acta Mechanica*, 1-16. https://doi.org/10.1007/s00707-025-04230-y

Zerrouki, R., Zidour, M., Tounsi, A., Tounsi, A., Belabed, Z., Bousahla, A.A., Salem, M.A. and Khedher, K.M. (2024), "Buckling behavior of nonlinear fg-cnt reinforced nanocomposite beam reposed on winkler/pasternak foundation", *Comput. Concr.*, **34**(3), 297. https://doi.org/10.12989/cac.2024.34.3.297

CC